Deterministic optical control of room temperature multiferroicity in $BiFeO_3$ thin films

Yi-De Liou[1], Yu-You Chiu[1], Ryan Thomas Hart[2], Chang-Yang Kuo[3,4], Yen-Lin Huang[5], Yuan-Chih Wu[1], Rajesh V. Chopdekar[6], Heng-Jui Liu[7], Arata Tanaka[8], Chien-Te Chen[4], Chun-Fu Chang[3], Liu Hao Tjeng[3], Ye Cao[2], Valanoor Nagarajan[9], Ying-Hao Chu[5,10,11], Yi-Chun Chen[1,12]* and Jan-Chi Yang[1,12]*

[1] *Department of Physics, National Cheng Kung University, Tainan 70101, Taiwan*
[2] *Department of Materials Science and Engineering, University of Texas at Arlington, Arlington, TX 76019, USA*
[3] *Max-Planck Institute for Chemical Physics of Solids, Dresden 01187, Germany*
[4] *National Synchrotron Radiation Research Center, Hsinchu 30076, Taiwan*
[5] *Department of Materials Science and Engineering, National Chiao Tung University, Hsinchu 30010, Taiwan*
[6] *Advanced Light Source, Lawrence Berkeley National Laboratory, Berkeley, CA 94720, USA*
[7] *Department of Materials Science and Engineering, National Chung Hsing University, Taichung 402, Taiwan*
[8] *Department of Quantum Matter, ADSM, Hiroshima University, Higashi-Hiroshima 739-8530, Japan*
[9] *School of Materials Science and Engineering, University of New South Wales, Sydney 2052, Australia*
[10] *Center for Emergent Functional Matter Science, National Chiao Tung University, Hsinchu 30010, Taiwan*
[11] *Institute of Physics, Academia Sinica, Taipei 11529, Taiwan*
[12] *Center for Quantum Frontiers of Research & Technology (QFort), National Cheng Kung University, Tainan 70101, Taiwan*

*e-mail: ycchen93@mail.ncku.edu.tw and janchiyang@phys.ncku.edu.tw

Abstract

Controlling ferroic orders (ferroelectricity, ferromagnetism, and ferroelasticity) by optical methods is a significant challenge due to the large mismatch in energy scales between order parameter coupling strengths and incident photons. Here, we demonstrate an approach to manipulate multiple ferroic orders in epitaxial mixed-phase $BiFeO_3$ thin film at ambient temperature via laser illumination. Phase-field simulations indicate that a light driven flexoelectric effect allows targeted formation of ordered domains. We also achieve precise sequential laser writing and erasure of different domain patterns, demonstrating deterministic optical control of multiferroicity at room temperature. As ferroic orders directly influence susceptibility and conductivity in complex materials, our results not only shed light on optical control of multiple functionalities but also suggest possible developments for opto-electronics and related applications.

Bismuth ferrite ($BiFeO_3$, BFO) is an archetypical room-temperature multiferroic[1] with coupled ferroelectric and antiferromagnetic order parameters, in which the spontaneous strain also accompanies the ferroelectricity. In bulk, the <111>-oriented ferroelectric polarization directly couples with the G-type antiferromagnetism as well as a weak ferromagnetic moment driven by Dzyaloshinskii–Moriya interaction[2,3]. Furthermore, the rotation of the ferroelectric polarization in BFO results in corresponding modulation of the (anti)ferromagnetism[4]. The demonstration of robust multiferroic properties in epitaxial BFO thin films, heralded as one of the breakthrough findings of the past decade[5], has opened several unforeseen device opportunities in oxide electronics technologies[6]. In addition to being sensitive to external stimuli such as stress[7], magnetic field[8], or electric field[5], BFO has tremendous potential in optoelectronic applications[9,10]**.** There has been an intense flurry of research activities focusing on electric field control of magnetism (and vice-versa) for BFO[11]. In contrast, reports on precise optical modulation of phase and structure of BFO, and hence functional responses remain scarce.

The deterministic control of electric, magnetic, and elastic orderings by means of light is not trivial. From an energy perspective, the scales for tailoring exchange coupling, spin-spin, and spin-orbital interactions range from few hundreds of μeV to meV[12-15], which are always significantly lower than the energy of a single photon in the visible spectrum (few eV). Such a huge energy mismatch typically inhibits precise manipulation of the ferroic orders under external light stimulus. Notwithstanding the above challenge, successful optical modulation of ferroic order parameters has been realized through tuning the complex interactions such as delicate combination of thermal effects, electronic excitation, phase stability, electrical field, and polarity of light[16-22]. In most cases, this is either done at low temperatures or with illumination by high-intensity pulsed lasers. Nevertheless, all-optical control of multiferroicity in a non-volatile way, especially at ambient temperature, has rarely been reported.

When proper in-plane compressive strain is applied to the epitaxial BFO film, it undergoes a phase transition to a mixed-phase system, which is composed of a tetragonal-like (T-BFO) and a

rhombohedral-like (R-BFO) BFO phases[23]. Mixed-phase BFO shows significant piezoelectricity[24] and enhanced magnetization[25]. The barrier for phase transition in this system is relatively low so that it can straddle easily across the R-T boundary under external stimuli[24] (typically exploited using either stress or electric field). The light-induced tuning of mixed-phase BFO could lead to the non-volatile optical control of multiferroicity, electromechanical response as well as the correlated magnetism, thus giving unprecedented device opportunities. In this study, we demonstrate distinct non-volatile manipulation of the phase and domain structures that exhibit coupled ferroic orders in mixed-phase BFO by light illumination. We find that the combination of light-induced thermal and flexoelectric effects effectively determines the domain transformation as well as the R-T phase distribution in mixed-phase BFO, enabling the deterministic control of corresponding ferroic orders.

Laser illumination on mixed-phase BFO

As the experimental setup illustrated in Fig. 1a, a 532 nm solid-state continuous wave laser (CW laser) is focused on the sample, where the power density is calibrated to be ~16 mW/μm^2. Fig. 1b and c show the topography of the mixed-phase BFO before and after laser illumination, respectively. The as-grown image shows irregular distribution of flat T-BFO and mixed-phase stripes composed of T-BFO and R-BFO. The light illumination results in the reconstruction of the as-grown mixed-phase feature as evidenced by the noticeable change in the illuminated region. For this region, T-BFO with a flat topography appears within the square region, while mixed-phase stripes form at the edge of illuminated area.

Having demonstrated that light-induced change in mixed-phase BFO is indeed possible, we next investigated the ferroelectric polarization as well as corresponding domain patterns after light illumination to reveal the key underpinning physical mechanisms. Note that in the case of the $BaTiO_3$ (BTO) single crystals, it was found that polarized light induced stress at the domain wall is the main cause behind the ferroelastic domain switching[21,22]. In the case of epitaxial BFO thin film system, more complexity arises from the additional in-plane polarization degrees of freedom[26-28]. Whilst the in-plane (IP) polarization components of R-BFO lies along the $<110>_{pc}$ axis, those of

T-BFO can be approximated to be along $<100>_{pc}$ directions at room temperature (here the pc refers to pseudo-cubic index). Thus, to simplify the case here, a well-aligned T-BFO domain with majority downward polarization component ($P_z \approx$ -1.4 C/m^2) and a small in-plane component ($P_{x,y} \approx$ 0.4 C/m^2), with ordered domain wall orientation lying along the $[110]_{pc}$ axis is first created using a biased scanning probe. The inset of Fig. 2a shows the in-plane piezoresponse force microscopy (IP PFM) image of the artificially created pure T-BFO background. After light illumination, the PFM images reveal that the direction of out-of-plane (OP) polarization of the light induced R- and T-BFO domains remains unchanged (Fig. 2b).

Using vector PFM analysis, the polarization of individual domains could be further revealed (see supplementary information Fig. S1), as labeled by the small colored arrows in Fig. 2a. For comparison, the individual and net polarization directions of untreated regions are also marked in Fig. 2a. Here the light induced T-BFO square created within the illuminated area splits into two triangular segments, each with different net in-plane (IP) polarizations, ie. $[110]_{pc}$ and $[\bar{1}\,\bar{1}0]_{pc}$, as indicated by the blue and red arrows in Fig. 2a. Note that the light induced T-BFO possesses the domain wall parallel to $[\bar{1}10]_{pc}$ axis and the net IP polarization pointing outward the illumination area (red and blue arrows), which shows a 90^o rotation with respect to the net IP polarization of non-illuminated area (green arrow). The PFM and topography images also reveal the new mixed-phase BFO stripes created at the boundaries of the illumination area for minimizing local elastic energy. To sum up our observation, the polarization configurations before and after light illumination are schematically illustrated in Fig. 2c and d.

It is noteworthy that a direct interaction between the electric field of the light and the spontaneous polarization is unlikely, given that the electric field of visible light oscillates at a much higher frequency (~10^{15} Hz) as compared to that of a ferroelectric dipole, unless nonlinear effects such as optical rectification are considered. To preclude the nonlinear effect of light, which usually exhibits angle dependent changes, we highlight that similar results could be obtained by using

different linearly and circularly polarized light under the same experimental setup (Fig. S2). This observation suggests the direct interaction between ferroelectric polarization and electric field of the incident light due to the non-linear effects has no dominant influence on the light-induced domain patterns. Through ultraviolet–visible and photoluminescence spectroscopies, we also learned that the illumination of a 532 nm laser would not generate significant amount of photo-excited carriers to drive the rotation of the ferroelectric polarization (Fig. S3). The observed light-driven phase and domain evolution of mixed-phase BFO could therefore be attributed to two possible mechanisms, i.e. photostrictive effect[10,29] or local heating[30]. However, the light induced photostrictive effect in BFO[10] is too small to provoke such a significant change. As a result, it is thought that the local heating effect might play the key role in driving the domain change.

Raman study during light illumination

To verify the role of local heating effect induced by light illumination, Raman spectroscopy was employed next to gain vital insight into details of (crystallographic) phase variation under light illumination. The power-dependent and temperature-dependent Raman spectra were taken for comparison, as shown in Fig. 3a and b, respectively. Note that the T-BFO exhibits a structure transformation from M_C tetragonal-like to M_A tetragonal-like phase at ~150 °C, accompanied by the in-plane rotation of polarization direction from $<100>_{pc}$ to $<110>_{pc}$[26], as illustrated in the inset of Fig. 3c (also refer to Fig. S4). When the phase transformation takes place, the characteristic phonon intensity of M_C phase T-BFO, at ~360 cm^{-1},[31] decreases along with increasing temperature. The laser induced heating can thus be calibrated by comparing the power-dependent and temperature-dependent spectra.

The strained BFO shows an anomalous change in phonon mode of ~360 cm^{-1} when laser power density is increased to the value of ~16 $mW/\mu m^2$, which is the power density adopted in Fig. 1 to drive the light-induced domain transformation. The decrease in intensity of characteristic phonon peak (360 cm^{-1}) with increasing laser power density indicates a gradual phase transition from M_C to M_A during light illumination. By further comparing the power-dependent and

temperature-dependent Raman spectra, it can be inferred that the effect of laser illumination is essentially the same as the effect of local heating. This comparison is also in nice agreement with temperature estimation deduced from Stokes–anti-Stokes ratio, as shown in Figure 3d (also refer to Fig. S5 and S6). The estimated local temperature with light illumination of 16 mW/um^2 is close to ~150 °C, at which the T-BFO tends to transform from M_C to M_A phase. This suggests the thermal effect is responsible to the presence of light-induced phase change and domain reconstruction in BFO; however, it still can't explain why the induced ferroelectric domains transform in such a highly ordered pattern after illumination.

Role of flexoelectricity and phase-field simulations

To further explore the mechanism of light-induced ferroelectric domain switching in BFO, we carried out phase-field simulation[32-35]. As illustrated the lattice expansion during light illumination in Fig. 4a, we model the light illumination effect by setting the temperature to a higher value and adding a lattice expansion induced strain in the centered illumination region (see Methods for details). We start from a single M_C phase BFO before light illumination, with P_z along $[00\bar{1}]$ and alternating P_x / P_y along $[\bar{1}00]$ / [010] directions, which forms 45^o oriented domain walls (Fig. 4b), in agreement with the experimental characterization (inset of Fig. 2a). Under light illumination, the induced vertical strain in the illumination region is deduced from the lattice expansion along $[001]_{pc}$ via x-ray diffraction (see Methods and Fig. S4 for details). Assuming that ε_{33} is proportional to the light intensity (Fig. S7), we assume a dome-like distribution of ε_{33} and σ_{33} (Fig. S8). The vertical strain induces in-plane strain gradient ($d\varepsilon_{33}/dx_{1,2}$) and flexoelectric field ($E_{1,2}^f$) are related via $E_{1,2}^f = f_{12}(\frac{d\varepsilon_{33}}{dx_{1,2}})$, (also refer to Methods) where $x_{1,2}$ and f_{12} are the in-plane directions and the transverse flexoelectric coupling coefficients. The induced flexoelectric field is oriented in radial direction from the center to the edges of the illumination region (see Fig. S8), while the simulated domain structure under this radial flexoelectric field is shown in Fig. 4c. In the bottom-right of the illumination region, the simulated domain patterns exhibit the exact arrangement with net

polarization pointing along $[110]_{pc}$ and $[\bar{1}\,\bar{1}\,0]_{pc}$ as what we observed in the experiment; while in the top-left of the illumination region, they remain the same as those in the unilluminated region. The discrepancy exists in the top-left simulated pattern as compared to experimental observation. This is possibly due to the reasons that the flexoelectric field may be slightly asymmetric in experiment because of the light-focusing geometry and local thermal equilibrium, enabling the bottom-right configuration to consume the top-left unchanged area.

To offer a more accessible simulation result after light illumination based on real experiment, we set the same flexoelectric field effectively pointing along the $[110]_{pc}$ /$[\bar{1}\,\bar{1}\,0]_{pc}$ directions in the illuminated region. The simulated equilibrium domain pattern is shown in Fig. 4d, which is, in a nice agreement with our experimental observation. For comparison, we also applied flexoelectric field along the $[\bar{1}\,10]_{pc}$ /$[1\,\bar{1}\,0]_{pc}$ directions in the illuminated region (see Fig. S9a-c). In this scenario, no new super-T phases are formed in the illuminated region. Since the net in-plane component of the initial M_C phase is along $[\bar{1}\,10]_{pc}$, it is easier to switch to either $[110]_{pc}$ or $[\bar{1}\,\bar{1}\,0]_{pc}$ directions by 90° (Fig. S9d, e), than to $[1\,\bar{1}\,0]_{pc}$ direction by 180° under radiative flexoelectric field. This explains why only certain domain orientations are preferred as observed in real experiments (Fig. 2a). Additionally, reference simulations with smaller flexoelectric field are performed (Fig. S10). Clearly no new T phase domain pattern inside the illumination region is observable. Our phase-field simulation indicates that local heat and flexoelectric effect are both important to the domain/phase reconfiguration during illumination.

In order to experimentally examine the existence of flexoelectricity, Kelvin probe force microscopy (KFM) is employed to map the potential energy profile after illumination. As shown in Fig. 4e and f, a ring-shape accumulation of negative charges is observed at the edge of the illuminated area, which indicates a radiative flexoelectric field is built under light illumination. The light induced strain gradient towards the center of the illumination area results in the creation of

198 flexoelectric polarization that is opposite to the strain gradient[36], as illustrated in Fig. 4a. As the
199 local region is heated up by light illumination, the generated hot carriers drift from the illuminated
200 region to the boundaries along with the flexoelectric field built up by the strain gradient, resulting in
201 the ring-like charge accumulation.

202 Fig. 4g schematically illustrates the evolution of the optically controlled domain formation.
203 The first step exploits the possible domain variants in T-BFO, where each can occur with sequential
204 rotation of polarization. The light induced phase transformation from M_C to M_A phase rotates the
205 polarization variants of each domain for 45^o, creating a metastable state during light illumination. In
206 the meanwhile, the flexoelectric effect takes place and builds up the flexoelectric field at the
207 illuminated area, leaving the polarizations pointing outward. As the light is turned off, the centered
208 BFO domains transform back to M_C tetragonal-like phase. Taking flexoelectric field and boundary
209 conditions of as-grown domains into consideration, the anisotropic build-in electric field results in
210 the perpendicular feature between the induced and original domain walls (Fig. 2d).

211 **Modification of correlated ferroic orders**

212 To investigate the correlated ferroic orders altered by light illumination, photoemission
213 electron microscopy (PEEM) and x-ray absorption spectroscopy (XAS) were performed at
214 BL11.0.1 at the Advanced Light Source, Berkeley Lab and at TPS45A NSRRC-MPI beamline at
215 Taiwan Photon Source (TPS), respectively (see Methods and Fig. S11 for details). Fig. 5a combines
216 the in-plane PFM and the corresponding x-ray linear dichroism (XLD)/x-ray circular dichroism
217 (XMCD) -PEEM images acquired at the same position. Our XLD experiment implemented at TPS
218 reveals the local antiferromagnetic Néel temperature (T_N) of T-BFO is significantly lower than that
219 of the R-BFO (Fig. S11). The spatially resolved XLD-PEEM image in Fig. 5a also shows that the
220 R-BFO among the mixed-phase stripes (shown in black contrast) has significantly stronger linear
221 dichroism contrast (due to antiferromagnetism) than the matrix, T-BFO (shown in gray contrast).
222 The image contrast in PEEM-XMCD is effectively a map of the local ferromagnetic order, in which
223 the areas that have their magnetic moments lying parallel to k-vector of the incident X-ray show red

contrast, whereas those that are antiparallel appear in blue contrast. By mapping the local magnetization, no magnetic moment is detectable above noise level in the T-BFO area, while the magnetic contrast could be clearly observed at the stripes created at the boundaries of the illumination area. This observation agrees with previous studies, in which the enhanced magnetization in mixed-phase stripe is attributed to the strained R-like BFO phase[25]. With these measurements taken as a whole, we can conclude that tuning the BFO domain structures and phase distribution via light stimulus is essentially controlling the correlated ferroelectricity, antiferromagnetism and remnant magnetization simultaneously.

Having understood the key factors underpinning light induced changes in BFO, macroscopic domain engineering can be achieved with proper control of the motion of the laser spot. Fig. 5b and c shows the schematic of the tuning feature and experimental demonstration of domain percolation via continually moving the laser spot, respectively. Fig. 5b illustrates the formation of a 'designer domain architecture' achieved by moving illumination spot. Moving the illumination spot along the different $<100>_{pc}$ directions effectively breaks the polarization symmetry. As a result, the orientation of domain pattern at the rear side of the moving illumination trajectory is always preferred, dominating the polarization of resultant domains. The presence of domain symmetry-breaking is similar to the electrical control of polarization in BFO mixed-phase system, enabling the preferred domain pattern determined by the moving tips[27,37]. In light of the antiferromagnetism and enhanced magnetization in BFO are closely related to the mixed-phase stripes, the light induced designer domain architectures can be seen as different non-volatile memory or function units.

Reversible optical control at ambient temperature

The optical tunability of the phases and complex domain architectures shown above for mixed-phase BFO (a morphotropic phase boundary (MPB) like piezoelectric material) makes it now possible to demonstrate the deterministic control of correlated phenomena. The MPB in piezoelectric materials is rich with unique physical properties, including large dielectric,

conductivity, significant piezoelectricity and enhanced elasto-optic effects[9,38-40]. Here, reversible modulation of the enhanced piezoelectricity is achieved by erasing and rewriting the T-BFO and MPB by means of light. Fig. 6a shows the AFM images taken at the same area after repeatedly illumination with controlled moving spot. The illumination center was focused on the blue circle as the first step (State 1), moved towards red triangle (State 2) and then returned to the blue circle once again (State 3). It could be seen that the BFO at blue point experiences an evolution from pure T-BFO to mixed-phase, and then back to pure T-BFO morphology after the third step. On the contrary, the red triangle region evolves from mixed-phase to pure T-BFO and back to mixed-phase. The piezoelectric coefficient, d_{33}, which quantifies the volume change of a piezoelectric material under electric field at blue circle and red triangle in each step are recorded accordingly, as plotted the piezoelectric hysteresis loop in Fig. 6b,c. The blue circle region shows an enhancement in d_{33} for 40 % when the T-BFO matrix is switched to mixed-phase state, while the reverse control is demonstrated when the region transforms to T-BFO once again, presenting a low-high-low (80-110-78 pm/V) d_{33} switching. On the other hand, the red triangle region behaves in an opposite trend, showing a high-low-high (112-72-115 pm/V) d_{33} sequence. In the same manner, the reversible optical control of electrical conductivity can also be carried out, taking advantage of the high conductivity occurring at T-R phase boundary in mixed-phase system (see Fig. S12).

Outlook

Our results successfully demonstrate the non-volatile and deterministic optical control of the multiferroic BFO at ambient temperature, a non-contact external control without any aid of applied electrical or magnetic fields. The illumination of laser spot results in well-defined domain patterns, driven by a decent combination of thermal and flexoelectric effects. Taking the advantage of the correlated order parameters, the ferroelectricity, antiferromagnetism and enhanced magnetization in BFO can be tuned simultaneously by means of light. Further symmetry-breaking is fulfilled by the motion of laser spot, giving rise to the artificial domain writing capability on macroscopic scale. The optical control of multiferroicity not only offers an effective approach to tailor the ferroic

orders in complex materials, but also a distinct direction towards technologically important applications such as non-volatile random access memories and data storage devices[6,41,42].

References

1. Fischer, P., Polomska, M., Sosnowska, I. & Szymanski, M. Temperature dependence of the crystal and magnetic structure of $BiFeO_3$. *J. Phys. Solid State Phys.* **13**, 1931-1940 (1980).
2. Dzialoshinskii, I. E. Thermodynamic theory of 'weak' ferromagnetism in antiferromagnetic substances. *Sov. Phys. JETP* **5**, 1259-1272 (1957).
3. Moriya, T. Anisotropic superexchange interaction and weak ferromagnetism. *Phys. Rev.* **120**, 91-98 (1960).
4. Zhao, T. *et al.* Electrical control of antiferromagnetic domains in multiferroic $BiFeO_3$ films at room temperature. *Nat. Mater.* **5**, 823-829 (2006).
5. Chu, Y. H. *et al.* Electric-field control of local ferromagnetism using a magnetoelectric multiferroic. *Nat. Mater.* **7**, 478-482 (2008).
6. Bibes, M. & Barthelemy, A. Multiferroics: Towards a magnetoelectric memory. *Nat. Mater.* **7**, 425-426 (2008).
7. Gao, P. *et al.* Ferroelastic domain switching dynamics under electrical and mechanical excitations. *Nat. Commun.* **5**, 3801 (2014).
8. Tokunaga, M. *et al.* Magnetic control of transverse electric polarization in $BiFeO_3$. *Nat. Commun.* **6**, 5878 (2015).
9. Sando, D. *et al.* Large elasto-optic effect and reversible electrochromism in multiferroic $BiFeO_3$. *Nat. Commun.* **7**, 10718 (2016).
10. Kundys, B., Viret, M., Colson, D. & Kundys, D. O. Light-induced size changes in $BiFeO_3$ crystals. *Nat. Mater.* **9**, 803-805 (2010).
11. Heron, J. T., Schlom, D. G. & Ramesh, R. Electric field control of magnetism using $BiFeO_3$-based heterostructures. *Appl. Phys. Rev.* **1**, 021303 (2014).
12. Jia, C., Onoda, S., Nagaosa, N. & Han, J. H. Microscopic theory of spin-polarization coupling in multiferroic transition metal oxides. *Phys. Rev. B* **76**, 144424 (2007).
13. Shalom, B. M., Sachs, M., Rakhmilevitch, D., Palevski, A. & Dagan, Y. Tuning spin-orbit coupling and superconductivity at the $SrTiO_3/LaAlO_3$ interface: A magnetotransport study. *Phys. Rev. Lett.* **104**, 126802 (2010).
14. Caviglia, A. D. *et al.* Tunable rashba spin-orbit interaction at oxide interfaces. *Phys. Rev. Lett.* **104**, 126803 (2010).
15. Chaloupka, J., Jackeli, G. & Khaliullin, G. Zigzag magnetic order in the iridium oxide Na_2IrO_3. *Phys. Rev. Lett.* **110**, 097204 (2013).
16. Stanciu, C. D. *et al.* All-optical magnetic recording with circularly polarized light. *Phys. Rev. Lett.* **99**, 047601 (2007).
17. Manz, S. *et al.* Reversible optical switching of antiferromagnetism in $TbMnO_3$. *Nat. Photon.* **10**, 653-656 (2016).
18. Lambert, C.-H. *et al.* All-optical control of ferromagnetic thin films and nanostructures. *Science* **345**, 1337-1340 (2014).
19. Kimel, A. V. *et al.* Ultrafast non-thermal control of magnetization by instantaneous

photomagnetic pulses. *Nature* **435**, 655-657 (2005).
20. Yang, M. M. & Alexe, M. Light-induced reversible control of ferroelectric polarization in $BiFeO_3$. *Adv. Mater.* **30**, 1704908 (2018).
21. Rubio-Marcos, F., Del Campo, A., Marchet, P. & Fernández, J. F. Ferroelectric domain wall motion induced by polarized light. *Nat. Commun.* **6**, 6594 (2015).
22. Rubio-Marcos, F. *et al.* Reversible optical control of macroscopic polarization in ferroelectrics. *Nat. Photon.* **12**, 29-32 (2018).
23. Zeches, R. J. *et al.* A strain-driven morphotropic phase boundary in $BiFeO_3$. *Science* **326**, 977-980 (2009).
24. Zhang, J. X. *et al.* Large field-induced strains in a lead-free piezoelectric material. *Nat. Nanotech.* **6**, 98-102 (2011).
25. He, Q. *et al.* Electrically controllable spontaneous magnetism in nanoscale mixed phase multiferroics. *Nat. Commun.* **2**, 225 (2011).
26. Liu, H. J. *et al.* Strain-driven phase boundaries in $BiFeO_3$ thin films studied by atomic force microscopy and x-ray diffraction. *Phys. Rev. B* **85**, 014104 (2012).
27. Chen, Y. C. *et al.* Electrical control of multiferroic orderings in mixed-phase $BiFeO_3$ films. *Adv. Mater.* **24**, 3070-3075 (2012).
28. You, L. *et al.* Characterization and manipulation of mixed phase nanodomains in highly strained $BiFeO_3$ thin films. *ACS Nano* **6**, 5388-5394 (2012).
29. Kundys, B. *et al.* Wavelength dependence of photoinduced deformation in $BiFeO_3$. *Phys. Rev. B* **85**, 092301 (2012).
30. Lo, H. W. & Compaan, A. Raman measurements of temperature during cw laser heating of silicon. *J. Appl. Phys.* **51**, 1565-1568 (1980).
31. Huang, Y. C. *et al.* Magnetic-coupled phase anomaly in mixed-phase $BiFeO_3$ thin films. *APL Mater.* **5**, 086112 (2017).
32. Li, Y. L., Hu, S. Y., Liu, Z. K. & Chen, L. Q. Phase-field model of domain structures in ferroelectric thin films. *Appl. Phys. Lett.* **78**, 3878-3880 (2001).
33. Xue, F., Li, Y. J., Gu, Y. J., Zhang, J. X. & Chen, L. Q. Strain phase separation: Formation of ferroelastic domain structures. *Phys. Rev. B* **94**, 220101 (2016).
34. Cao, Y. *et al.* Exploring polarization rotation instabilities in super-tetragonal $BiFeO_3$ epitaxial thin films and their technological implications. *Adv. Electron. Mater.* **2**, 1600307 (2016).
35. Li, Q. *et al.* Giant elastic tunability in strained $BiFeO_3$ near an electrically induced phase transition. *Nat. Commun.* **6**, 8985 (2015).
36. Kalinin, S. V. & Morozovska, A. N. Multiferroics: Focusing light on flexoelectricity. *Nat. Nanotech.* **10**, 916-917 (2015).
37. Balke, N. *et al.* Deterministic control of ferroelastic switching in multiferroic materials. *Nat. Nanotech.* **4**, 868-875 (2009).
38. Shrout, T. R., Chang, Z. P., Kim, N. C. & Markgraf, S. Dielectric behavior of single crystals near the $_{(1-x)}Pb(\ Mg_{1/3}\ Nb_{2/3}\ )O_{3-(x)}$ $PbTiO_3$ morphotropic phase boundary. *Ferroelectr. Lett.* **12**,

63-69 (1990).
39. Eitel, R. E. *et al.* New high temperature morphotropic phase boundary piezoelectrics based on $Bi(Me)O_3$-$PbTiO_3$ ceramics. *Jpn. J. Appl. Phys.* **40**, 5999-6002 (2001).
40. Chu, K. *et al.* Enhancement of the anisotropic photocurrent in ferroelectric oxides by strain gradients. *Nat. Nanotech.* **10**, 972-979 (2015).
41. Garcia, V. & Bibes, M. Ferroelectric tunnel junctions for information storage and processing. *Nat. Commun.* **5**, 4289 (2014).
42. Slaughter, J. M. Materials for magnetoresistive random access memory. *Annu. Rev. Mater. Res.* **39**, 277-296 (2009).

Acknowledgements

This work is supported by the Ministry of Science and Technology (MOST) in Taiwan, under Grant Nos. MOST 107-2636-M-006-003 (Young Scholar Fellowship Program), 105-2112-M-006-001-MY3, 106-2119-M-009-011-MY3, 106-2628-E-009-001-MY2, and 107-2627-E-006-001. Y.H.C acknowledges the financial support from Academia Sinica, Taiwan (iMATE-107-11) and Center for Emergent Functional Matter Science at National Chiao Tung University. R.T.H and Y.C. acknowledge the Texas Advanced Computing Center (TACC) at The University of Texas at Austin for providing HPC resources that have contributed to the research results reported within this paper (URL: http://www.tacc.utexas.edu). C.Y.K., C.T.C., C.F.C., and L.H.T. acknowledge support from the Max-POSTECH/Hsinchu Center for Complex Phase Materials, and thank H.-M. Tsai, H.-W. Fu and C.-Y. Hua for their skillful technical assistance. This research used resources of the Advanced Light Source, which is a DOE Office of Science User Facility under contract no. DE-AC02-05CH11231.

Author contributions

J.C.Y., Y.L.H. and Y.H.C. processed the sample growth. Y.D.L. and Y.Y.C. conducted the laser illumination, Raman spectroscopy and scanning probe microscopy, and analyzed the data. R.T.H and Y.C. conducted the phase-field simulation. Y.C.W and H.J.L processed x-ray reciprocal mapping and resolved the phase transformation at elevated temperature. R.V.C. acquired and analyzed PEEM results. C.Y.K, C.T.C., A.T., C.F.C. and L.H.T measured and analyzed XAS and XLD, and conducted cluster calculation. V.N. analyzed the PFM data and provided guidance on related experiments. Y.C.C. and J.C.Y. conceived the idea, led the project, analyzed data and co-wrote the paper. All authors contributed to the manuscript.

Competing Interests

The authors declare no competing interests.

Additional Information

Supporting Information is available online.

Correspondence and requests for materials should be addressed to Y. C. Chen or J. C. Yang.

Methods

Sample growth

The mixed-phase BFO film with thickness of 120 nm was deposited on the conductive $LaNiO_3$ (LNO) buffered (001) $LaAlO_3$ (LAO) substrates via pulsed laser deposition (Mobile Combi-Laser MBE MC-LMBE, Pascal Co, Ltd.). A KrF excimer laser was employed to strike a stoichiometric BFO target at a laser repetition rate of 10 Hz. The growth temperature was fixed at 700°C with an oxygen pressure of 100 mTorr. After the deposition, the films were cooled in 1 atm of oxygen. Reflection high energy electron diffraction was used to *in-situ* monitor the growth.

Illumination setup

The optical modulation process was performed via micro Raman spectroscope with 532 nm solid-state continuous wave (CW) laser as the excited source. The laser beam was then focused into a spot size with diameter of 2 μm by a 100X objective lens (NA = 0.95). The incident laser power was precisely controlled by an attenuation-adjustable neutral density filter. The Stokes/Anti-Stokes-shifted Raman spectra were collected via confocal backscattering-based detection in ambient environment and then analyzed by spectrometer (iHR550, Horiba Jobin Yvon) with spectra resolution ~0.74 cm^{-1}. A high-precision step-motor stage (Tango desktop, MÄRZHÄUSER WETZLAR) was used to control the motion of the samples.

Scanning probe characterization

The images of surface topography, piezoresponse force microscopy (PFM), surface potential (measured by Kelvin probe force microscopy, KPFM) and conductive atomic force microscopy (C-AFM) were recorded by a commercial scanning probe microscope system (multimode 8, Bruker) using commercial Pt-Ir coated probe with elastic constants about 7 N/m. During the PFM imaging, ac voltage with amplitude of 1 V and frequency of 7 kHz was applied to the probe and the direction of cantilever was parallel to the [010] crystalline axis of the T-BFO matrix.

Phase-field modeling

In the phase-field simulation, polarization vector $P_i=(P_1,P_2,P_3)$ was chosen as the order parameter to describe the ferroelectric state in $BiFeO_3$ thin film. The temporal evolution of P_i is governed by the time-dependent Landau-Ginzburg-Devonshire (LGD) equations,

$$\frac{\partial P_i(\boldsymbol{x},t)}{\partial t}=-L\frac{\delta F}{\delta P_i(\boldsymbol{x},t)},(i=1\sim 3) \qquad (1)$$

where $\boldsymbol{x}$ is the spatial position, t is the time, L is the kinetic coefficient related to the domain wall mobility. The total energy of the system (F) is expressed as a volume integral of total free energy density (f), i.e., $F=\int_V f dV$, in which f includes the Landau free energy density (f_{land}), the gradient energy density (f_{grad}), the elastic energy density (f_{elast}), the electrostatic energy density (f_{elec}) and the flexoelectric energy density (f_{flexo}). Detailed expressions of each free energy density can be found in literature[43,44]. Equation (1) is numerically solved using a semi-implicit spectral method based on a 3D geometry sampled on a $256\Delta x\times256\Delta x\times36\Delta x$ system size, with Δx =1.0nm. The thickness of the film, substrate and air are $20\Delta x$, $10\Delta x$ and $2\Delta x$ respectively. The isotropic relative dielectric constant (κ_{ii}) is chosen to be 50. The gradient energy coefficients are set to be $G_{11}/G_{110}=1.0$, $G_{12}/G_{110}=0.0$, $G_{44}/G_{110}=0.5$ while $G_{110}=1.73\times10^{-10}C^{-2}m^4N$. The biaxial substrate strain is set to be -4.5% based on the lattice mismatch between the $BiFeO_3$ film and $LaAlO_3$ substrate. The Landau energy coefficients, electrostrictive coefficients and elastic compliance constants are collected from literature[45,46]. In all the Landau energy coefficients (α's)

only α_1 is temperature dependent. Based on the Curie-Weiss law it is written as $\alpha_1(r)=[T(r)-T_0]/(2\varepsilon_0 C)$, in which r is the position, T_0 is the Curie temperature, ε_0 is the dielectric permittivity of vacuum, C is the Curie constant, and $T(r)$ is the position-dependent temperature. To model the laser illumination on the center area of the BFO thin film, we set $T(r)$ to be,

$$T(r)=\begin{cases} T_{\text{illumin}} & (r \le a) \\ 298\text{K} & (r > a) \end{cases} \quad (2)$$

where $r=\sqrt{(x-x_0)^2+(y-y_0)^2}$ is the distance from the illumination center (x_0,y_0), and a (=64Δx) is the radius of the illuminated region. The light induced vertical strain (ε_{33}) is assumed to be in a dome-like distribution (Fig. S8) according to the measured light intensity profile (Fig. S7), it is written as,

$$\varepsilon_{33}(r)=\begin{cases} \varepsilon_{33}^{center}\sqrt{1-\dfrac{r^2}{r^2}} & (r \le a) \\ 0 & (r > a) \end{cases} \quad (3)$$

where $\varepsilon_{33}^{center}$ represents the maximum vertical strain in the center of the illumination region. It is approximated from the lattice expansion along $[001]_{pc}$ direction, i.e., $\varepsilon_{33} = (c_{T2} - c_{T1}) / c_{T1}$, where c_{T1} and c_{T2} are the experimentally measured lattice constants of the super-T phase before and after the illumination (supplementary information Fig. S4). In our simulation, the light-induced in-plane strains (ε_{11}, ε_{22}) are negligible due to the substrate constraint. The flexoelectric energy density (f_{flexo}) can be written as a function of polarization (P_i) and its spatial gradient (∇P), as well as strain (ε_{kl}) and its spatial gradient ($\nabla\varepsilon_{kl}$),

$$f_{flexo}(P_i,\varepsilon_{kl},\nabla P_i,\nabla\varepsilon_{kl})=\frac{1}{2}f_{ijkl}\left(\frac{\partial P_k}{\partial x_l}\varepsilon_{ij}-\frac{\partial \varepsilon_{ij}}{\partial x_l}P_k\right)=\frac{1}{2}F_{ijkl}\left(\frac{\partial P_k}{\partial x_l}\sigma_{ij}-\frac{\partial \sigma_{ij}}{\partial x_l}P_k\right) \quad (4)$$

in which f_{ijkl} (unit: V) and F_{ijkl} (unit: Vm^2N^{-1}) are the flexoelectric coupling coefficient (FCC) tensors, which are related through $f_{ijkl}=c_{ijmn}F_{mnkl}$. The effect of flexoelectric energy on the polarization evolution is modeled by minimizing f_{flexo} over P_k,

$$\frac{\delta f_{\text{flexo}}}{\delta P_k}=\frac{\partial f_{\text{flexo}}}{\partial P_k}-\frac{\partial}{\partial x_l}\frac{\partial f_{\text{flexo}}}{(\partial P_k/\partial x_l)}=-F_{ijkl}\frac{\partial \sigma_{ij}}{\partial x_l}=-E_k^f \quad (5)$$

For cubic symmetry the flexoelectric coupling coefficient tensor has three independent components, i.e., F_{1111}, F_{1122} and F_{1221}.[47-49] By using Voigt notation $F_{11}=F_{1111}$, $F_{12}=F_{1122}$ and $F_{44}=2F_{1221}$, Eq. (5) can be expanded as,

$$E_1^f = F_{11}\frac{\partial \sigma_1}{\partial x_1} + F_{12}(\frac{\partial \sigma_2}{\partial x_1} + \frac{\partial \sigma_3}{\partial x_1}) + F_{44}(\frac{\partial \sigma_5}{\partial x_3} + \frac{\partial \sigma_6}{\partial x_2})$$

$$E_2^f = F_{11}\frac{\partial \sigma_2}{\partial x_2} + F_{12}(\frac{\partial \sigma_3}{\partial x_2} + \frac{\partial \sigma_1}{\partial x_2}) + F_{44}(\frac{\partial \sigma_6}{\partial x_1} + \frac{\partial \sigma_4}{\partial x_3}) \quad (6)$$

$$E_3^f = F_{11}\frac{\partial \sigma_3}{\partial x_3} + F_{12}(\frac{\partial \sigma_1}{\partial x_3} + \frac{\partial \sigma_2}{\partial x_3}) + F_{44}(\frac{\partial \sigma_4}{\partial x_2} + \frac{\partial \sigma_5}{\partial x_1})$$

We made assumption that the light-induced strain and stress are confined along $[001]_{pc}$ direction, which gradually decrease from the illumination center to the edges. The variation of strain and stress along the $[001]_{pc}$ direction are neglected. Based on these assumptions and according to Eq. (6), the vertical stress induces an in-plane stress gradient ($\partial\sigma_3 / x_{1,2}$) and flexoelectric field ($E_{1,2}^f$), i.e., $E_{1,2}^f = F_{12}(\partial\sigma_3 / x_{1,2})$, where $x_{1,2}$ and F_{12} are the in-plane directions and the transverse flexoelectric coupling coefficients. The flexoelectric coupling coefficients are chosen to be $f_{ij} = 10\text{V}$ or $F_{ij} = 1.0\times10^{-10}\,\text{Vm}^2\text{N}^{-1}$. They are estimated from the literature[50].

Photoemission electron microscopy

X-ray imaging with variable linear and circular polarization at the Fe *L* edges was performed at the PEEM3 endstation of BL11.0.1 at the Advanced Light Source, Berkeley Lab. The sample is held at an angle of 60 degrees with respect to the surface normal, and was mounted such that the x-rays are incident along the in-plane $[\bar{1}00]_{pc}$ direction. For all images, the x-ray incidence direction is from the right. The sample was held at a voltage of -18 kV to accelerate the photo-emitted and secondary electrons, proportional to the local x-ray absorption coefficient, through a series of electrostatic lenses towards a phosphor-coated fiber bundle coupled to a Peltier-cooled CCD detector. This allows spatial mapping of the polarization dependent x-ray absorption coefficient with a spatial resolution at or better than 50 nm. To probe antiferromagnetic and ferroelectric axis orientation projections along the x-ray linear polarization axis, linear dichroism images at the Fe L_2 A and B edges of 720.6 eV and 722 eV were taken first with x-ray polarization in the plane of the sample parallel to the [010] axis (s polarization), then with polarization nearly out of plane (p polarization). To enhance the ferroic contrast and to minimize topographic and work function contrast, the difference images of the L_2 A and B images were taken, then the ratio between s and p polarization difference images were used in Fig. 5a. For mapping the ferromagnetic domain contrast, the Fe L_3 A and B energies at 707.4 eV and 708.3 eV were used with right and left circular x-ray polarization. The difference between right and left circular polarization at each energy gives the projection of magnetization along the x-ray incidence direction, showing strong contrast for domains along the in-plane [100] and $[\bar{1}00]$ directions, and no sensitivity to magnetization along the in-plane [010] and $[0\bar{1}0]$ directions.

Data availability

The data supporting the findings of this study are available within the article and its supplementary files and available from the authors upon reasonable request.

References

43. Cao, Y., Chen, L. Q. & Kalinin, S. V. Role of flexoelectric coupling in polarization rotations at

the a-c domain walls in ferroelectric perovskites. *Appl. Phys. Lett.* **110**, 202903 (2017).
44. Gu, Y. *et al.* Flexoelectricity and ferroelectric domain wall structures: Phase-field modeling and DFT calculations. *Phys. Rev. B* **89**, 174111 (2014).
45. Cao, Y. *et al.* Exploring polarization rotation instabilities in super-tetragonal $BiFeO_3$ epitaxial thin films and their technological implications. *Adv. Electron. Mater.* **2**, 1600307 (2016).
46. Xue, F., Li, Y., Gu, Y., Zhang, J. & Chen, L. Q. Strain phase separation: Formation of ferroelastic domain structures. *Phys. Rev. B* **94**, 220101 (2016).
47. Quang, H. L. & He, Q. C. The number and types of all possible rotational symmetries for flexoelectric tensors. *Proc. Royal Soc. A* **467**, 2369-2386 (2011).
48. Shu, L., Wei, X., Pang, T., Yao, X. & Wang, C. Symmetry of flexoelectric coefficients in crystalline medium. *J. Appl. Phys.* **110**, 104106 (2011).
49. Shu, L., Wei, X., Pang, T., Yao, X. & Wang, C. Symmetry of flexoelectric coefficients in crystalline medium. *J. Appl. Phys.* **116**, 129901 (2014).
50. Zubko, P., Catalan, G. & Tagantsev, A. K. Flexoelectric effect in solids. *Annu. Rev. Mater. Res.* **43**, 387-421 (2013).

Figures

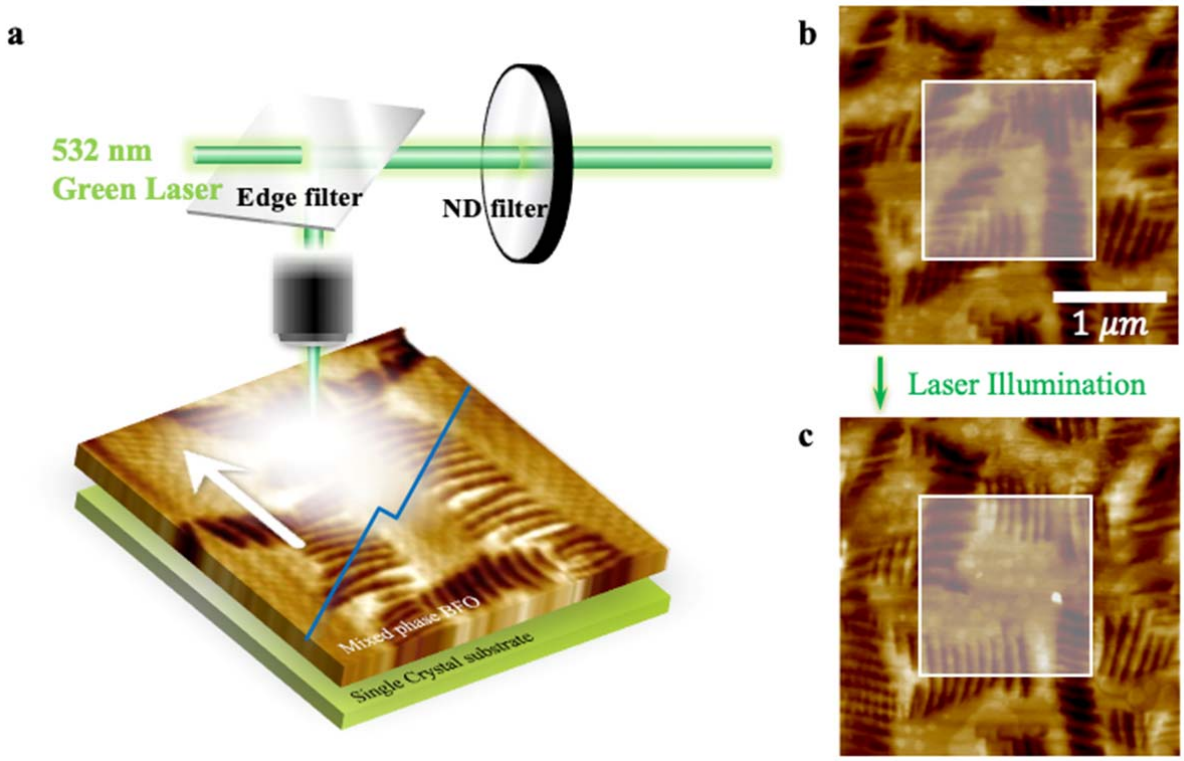

Fig. 1 Optical modulation of the highly-strained BFO thin film. a, Experiment setup of a double-stage green-laser-based (532 nm) illumination system, in which a attenuation-adjustable neutral density filter (ND filter) is used to offer precise control on the laser intensity. **b,** Topography image of an as-grown mixed-phase BFO thin film. **c,** Topography image of the same area after light illumination, showing a clear phase redistribution of T-like and R-like BFO phases. The white square indicates the illuminated area.

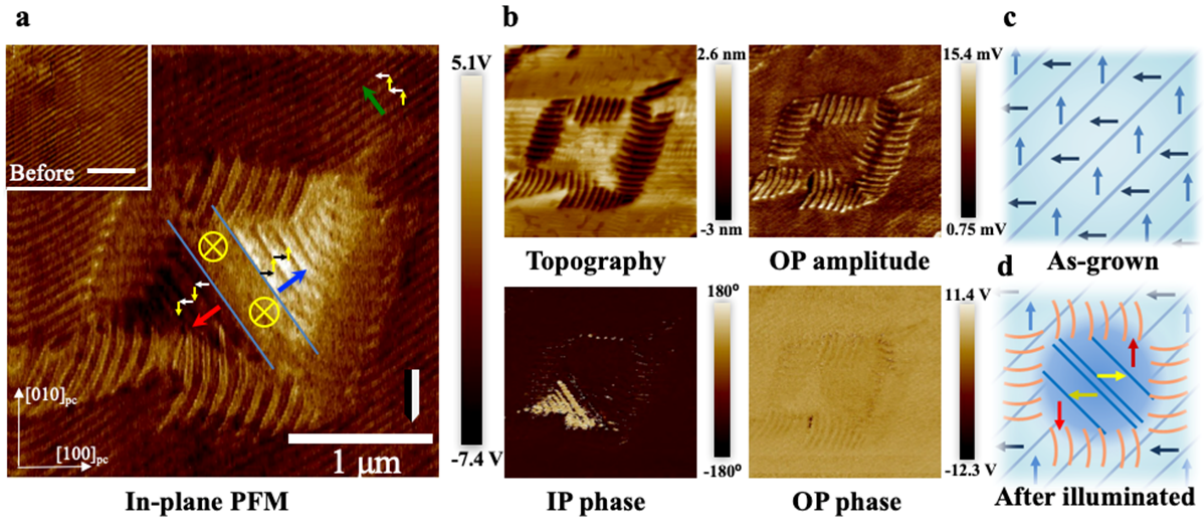

Fig. 2 The Ferroelectric configuration of a highly-strained BFO thin film after light illumination. a, In-plane (IP) PFM image of the light induced domain structure. The directions of the IP polarization of as-grown and induced T-BFO domains are marked by the small colored arrows in the image. The yellow, black and white arrows represent the T-BFO domain with in-plane polarization pointing along $[010]_{pc}/[0\bar{1}0]_{pc}$, $[100]_{pc}$ and $[\bar{1}00]_{pc}$, respectively, as identified by scanning cantilever parallel to [010]. The bold arrows (red, blue and green) indicate the net IP polarization directions. The inset shows the IP PFM image of the initial T-BFO domain matrix. **b,** Topography, IP and out-of-plane (OP) PFM taken in the same area. The original downward polarization is presented in OP bright contrast. **c,** Schematics of the domain variation in IP polarizations before and after laser illumination.

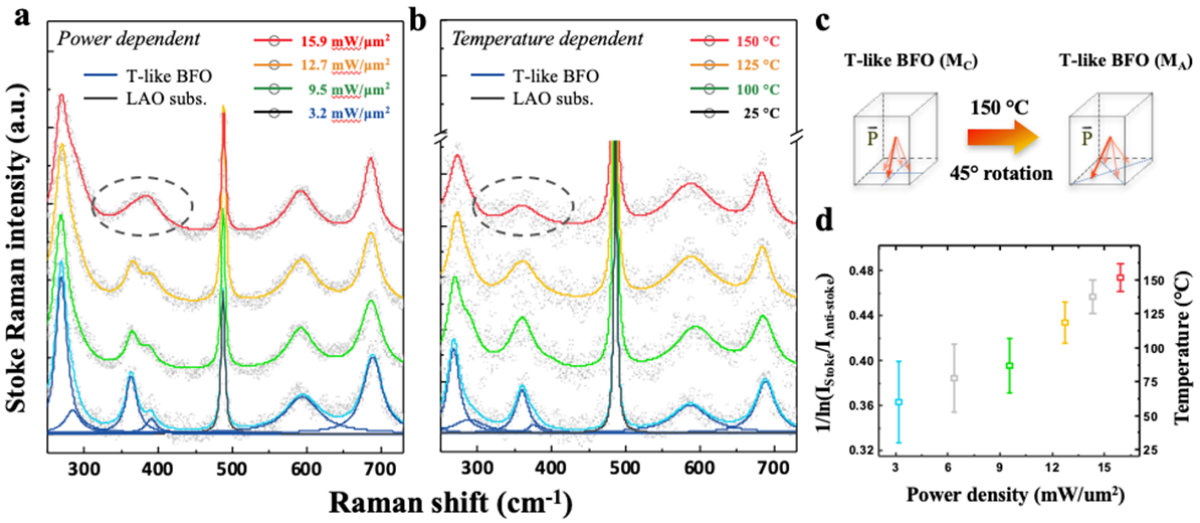

Fig. 3 Raman scattering study on the illuminated area. a,b, Power-dependent (**a**) and temperature-dependent (**b**) Raman spectra of mixed-phase BFO film. The weakened and broaden feature of phonon mode ~364 cm^{-1} of T-BFO is observed in both spectra due to structure phase transition, which corresponds the power density of 15.9 $mW/\mu m^2$ to local heating temperature of ~150°C. Detailed analysis of peak evolution during phase transition is provided in supporting information (Fig. S5). **c,** Schematic of T-BFO phase transition at 150°C, at which the monoclinic M_C phase transforms to M_A phase, accompanying a 45 degree rotation of polarization. **d,** Local heating temperature estimated by Stokes/Anti-stokes ratio of 689 cm^{-1} Raman band of T-BFO. The error bar is calculated by considering the signal-to-noise ratio based on different illumination condition. The detailed information related to the temperature estimation is described in supporting information (Fig. S6)

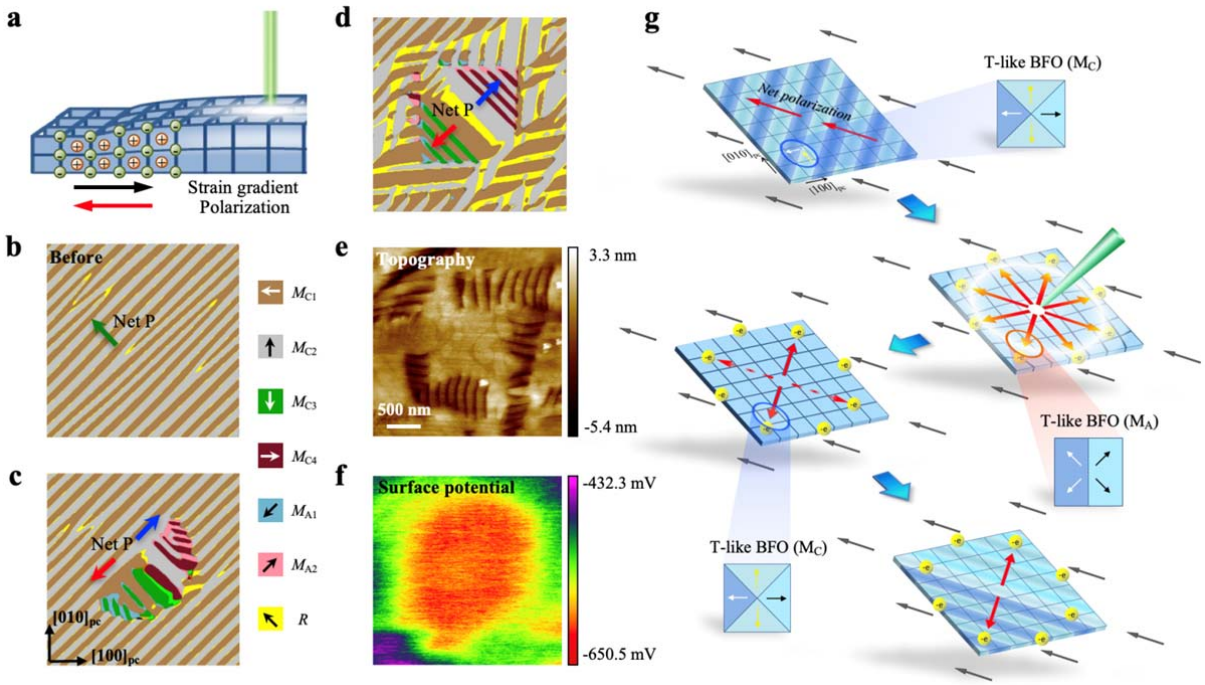

569

570 **Fig. 4 Phase-field simulations and flexoelectric effect under illumination. a**, Schematic of strain
571 gradient induced flexoelectric polarization under illumination. **b-d** Phase-field simulation on
572 domain structures of highly-strained BFO. (**b)** The simulated domain structure before light
573 illumination, where the green arrow indicates the net in-plane polarization. (**c**) Simulated
574 equilibrium domain structure under dome-like strain/stress distribution in the illuminated area. (**d**)
575 Simulated equilibrium domain structure when the induced flexoelectric field effectively points
576 along $[110]_{pc}$ /$[\bar{1}\,\bar{1}\,0]_{pc}$. The red and blue arrows in (**c**) and (**d**) indicate the net in-plane polarization
577 of the switched T-BFO. **e,** Topography and **f,** corresponding surface potential image take at the same
578 illuminated region. **g,** Schematic illustration of light-induced domain formation driven by the
579 combination of laser heating and flexoelectric effect. In (**g**), the bold arrows in black and red colors
580 present the net in-plane polarizations of non-illuminated and illuminated area, respectively. The
581 short colored arrows in the extended sketches show the possible in-plane polarization variants of
582 M_C and M_A BFO phases. The radiative orange arrows represent the effective flexoelectric field,
583 which drift the hot carriers from the photo-excited region to the illumination boundaries.

584

585

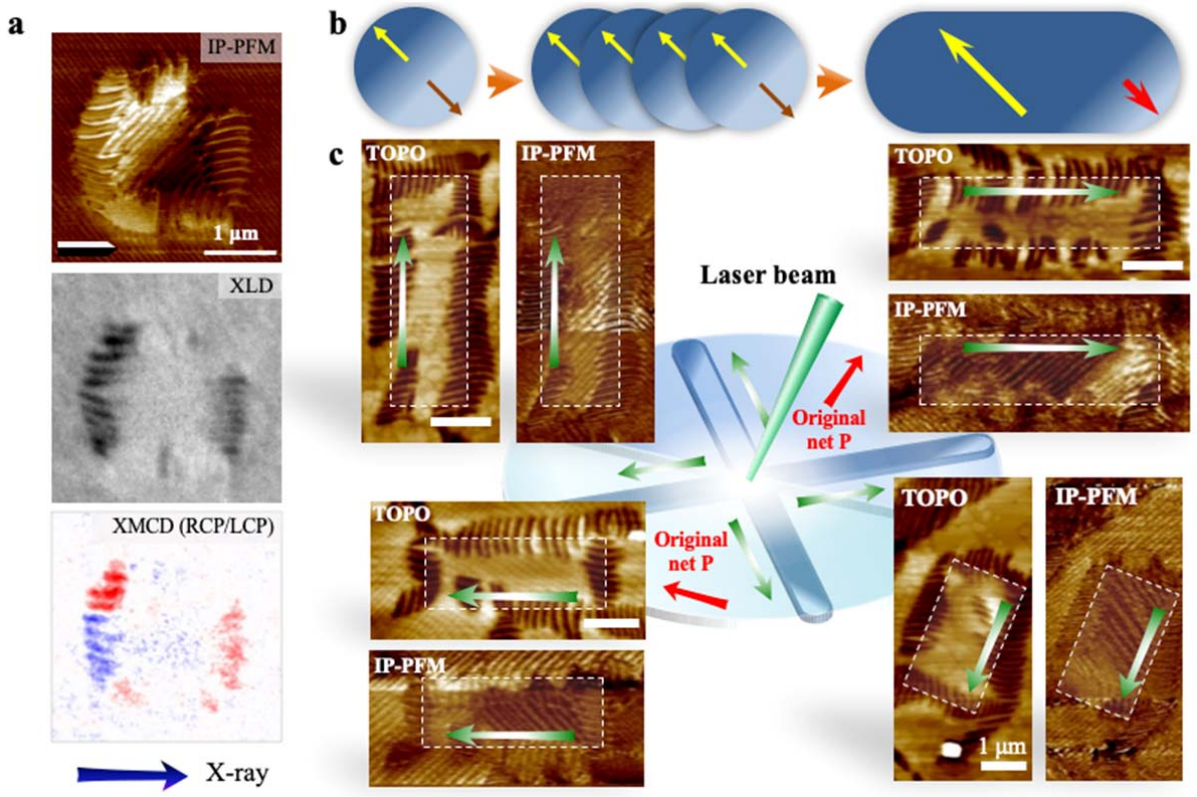

Fig. 5 Optical control of room-temperature multiferroicity in BFO and creating designer domain architectures via laser-spot motion. a, IP PFM and XLD/XMCD-PEEM images taken at the same illuminated region. Strong black and white contrast in the XLD-PEEM image indicates the strong dichroism resulting from antiferromagnetic order of BFO; while the red/blue contrast in XMCD-PEEM image show the existence of ferromagnetic moments lying parallel/antiparallel to k-vector of the incident X-ray, respectively. **b,** Schematics of the optical driven domain transformation and domain percolation with continually moving light spot towards right hand side. The yellow and brown arrows indicate the net in-plane polarization in the center of illumination spot, while green arrow indicates the moving direction of the laser spot. The in-plane electric fields of domains at rear parts of the illumination trajectory determine the polarization preference of resultant domains. **c,** Experimental demonstration of optical controlled designer domain architectures by moving the light spot along $<100>_{pc}$ directions.

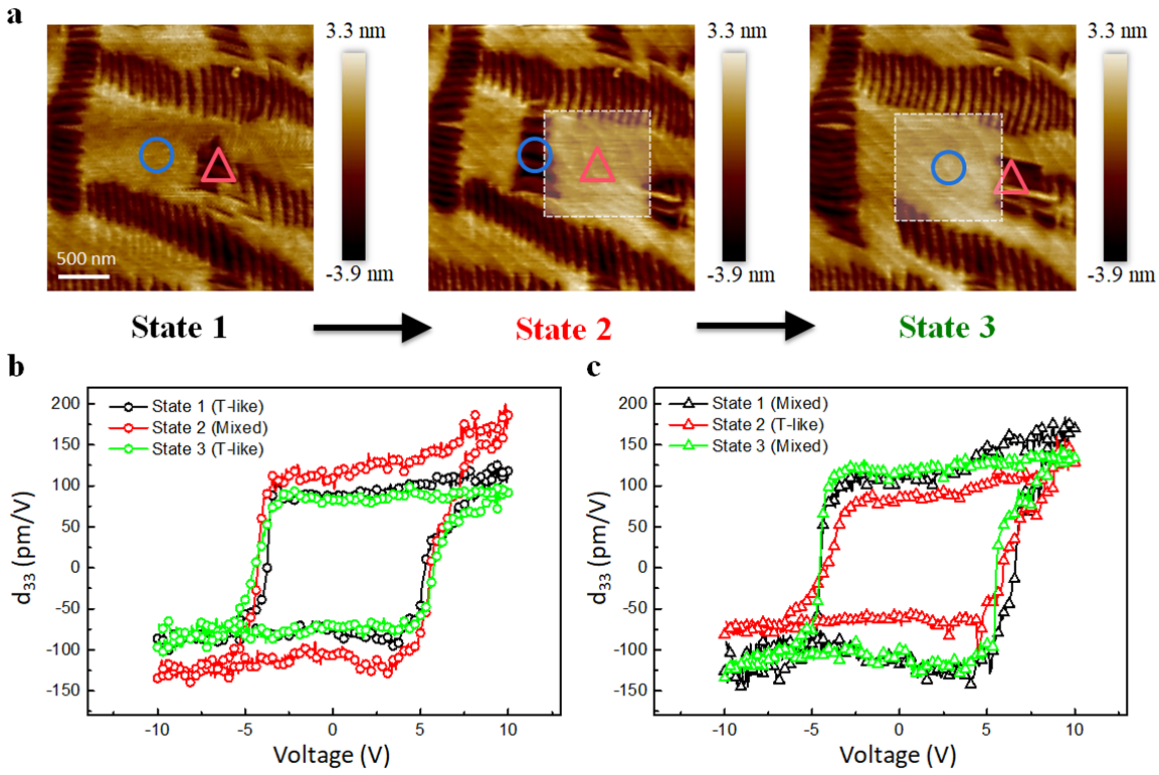

Fig. 6 Deterministic optical control of piezoelectric property in mixed-phase BFO. a, Topography images of mixed-phase BFO after repeatedly illumination taken in the same area. The d_{33} loop measured **b,** at blue circle and **c,** at red triangle with respect to state 1, 2 and 3. An enhanced d_{33} value can be observed with the formation of mixed-phase state, while a lower d_{33} value is obtained at the location of T-BFO.